State estimation for real-time analysis of dynamic plasma properties and electrical circuit effects in Hall effect thrusters

IEPC-2022-323

Daniel E. Troyetsky[1]
Stanford University, Stanford, California 94305, USA

Christine M. Greve[2]
Texas A&M University, College Station, Texas 77843, USA

Sedina Tsikata[3]
ICARE, Centre National de la Recherche Scientifique (CNRS), 45071 Orléans, France

Kentaro Hara[4]
Stanford University, Stanford, California 94305, USA

A major focus of current Hall effect thruster research is understanding the differences in performance between in-space and ground-testing operation. Two significant challenges in characterizing these differences are the poorly understood physics surrounding anomalous electron transport and the coupling between the thruster discharge plasma and the electrical configuration of the test facility. To investigate the influences of these processes on thruster performance without a priori knowledge of the dynamics governing anomalous transport, a physics-constrained extended Kalman filter is developed to estimate the dynamic behavior of plasma properties using experimentally-obtained discharge current signals as a measurement. A zero-dimensional global plasma ionization oscillation model and lumped-element circuit model form the dynamics model that applies the constraints to the filter. More specifically, ion and neutral number densities, ion and electron bulk velocities, electron temperature, anode voltage, and discharge filter capacitor current are estimated. The behaviors of the states are compared with and without the ion momentum equation which predicts ion bulk velocity, as well as coupled and decoupled from the electrical circuit model.

I. Nomenclature

A_c	=	thruster cross-sectional area
C_f	=	facility capacitance
E	=	electric field strength
e	=	fundamental charge
F	=	dynamics model Jacobian
f	=	dynamics model function
G	=	noise gain matrix
H	=	measurement Jacobian matrix

[1] Graduate Student, Aeronautics and Astronautics, dtroyets@stanford.edu.
[2] Ph.D Graduate, Aerospace Engineering, cgreve@tamu.edu.
[3] Researcher, Electric Propulsion Team, sedina.tsikata@cnrs-orleans.fr.
[4] Assistant Professor, Aeronautics and Astronautics, kenhara@stanford.edu.

h	=	measurement vector
I_C	=	capacitor current
K	=	Kalman gain
L_{ch}	=	channel length
L_f	=	facility inductance
M_i	=	ion mass
$\dot{m}$	=	neutral mass flow rate
m_e	=	electron mass
N_i	=	ion number density
N_{int}	=	injected neutral number density at anode
N_n	=	neutral number density
P	=	system covariance
Q	=	process noise covariance
R	=	measurement noise covariance
R_f	=	facility resistance
R_Δ	=	channel width
S_j	=	electron energy gain due to Joule heating
S_w	=	electron energy loss due to wall collisions
S_c	=	electron energy loss due to inelastic ion collisions
T_e	=	electron temperature
U_e	=	electron bulk velocity
U_i	=	ion bulk velocity
$U_{i,w}$	=	ion acoustic speed
U_n	=	neutral bulk velocity
V_A	=	anode voltage
V_d	=	discharge voltage
x	=	state vector
$\tilde{y}$	=	measurement
ϵ_{ion}	=	ionization energy loss
ϵ_w	=	electron energy loss to the wall
ζ_{ion}	=	ionization rate coefficient
ν_w	=	electron wall collision frequency
χ	=	ionization cost
σ	=	rate of secondary electron emission
ϕ_w	=	sheath potential

II. Introduction

Hall effect thrusters (HETs) are plasma-based propulsion devices which are well-suited for long-duration and deep-space missions due to their high efficiency. Though these devices have been studied for decades, aspects of the underlying physics which govern their discharge plasma remain elusive and fully-predictive models of their behavior have yet to be developed. One obstacle towards developing predictive simulations is the presence of a wide range of oscillations in the discharge plasma, which exist in different spatial dimensions (e.g., axial or azimuthal), occur at different frequencies, and have different physical origins. Indicators of these different oscillations can often be detected in discharge current measurements [1–3].

While the discharge plasma in HETs is time-varying in nature, steady-state assumptions are often applied to electron momentum in simulations, assuming that collisional processes dominate inertial effects [4–6]. Past theoretical [7] and experimental [8–10] studies have provided evidence that these assumptions may be invalid in the case of the HET. Additional work by Wei et al. [11] has demonstrated that thruster performance can change significantly during a single breathing mode period, and a study by Mullins et al. [12] has provided experimental evidence of a change in amplitude and location of the Hall current, further emphasizing the significance of dynamic electron behavior.

One particular challenge is in understanding the anomalous enhancements to electron transport and diffusion across magnetic field lines, which have been shown to vary in time with the breathing mode [13]. Past attempts to describe this transport as being due to wall collisions [14], enhanced diffusion [15], plasma turbulence [16–18], or more likely,

a combination of factors, has been met with limited success. Though aspects of these theories have aligned with experimental observation, none have managed to entirely capture the observed behavior [19, 20]. Because anomalous transport plays an important role in governing device behavior and performance, incorrect approximations of its steady and time-varying magnitude may lead to significant errors.

Even if a model is developed which successfully describes the anomalous transport observed in experiments, the question remains whether this behavior will be the same as that observed during in-space operation. Past experimental works have demonstrated that a close coupling exists between the behavior of a HET discharge plasma and the electrical configuration of the test facility. Work by Frieman et al. [21] and Walker et al. [22] demonstrated close correlation between HET discharge current and the current collected on witness plates in a vacuum test facility. Peterson et al. observed that the breathing mode frequency varies depending on the potential of the thruster body [23]. Piñero investigated the role of harness impedance and discharge filter capacitance on anode voltage oscillations [24]. Combined, these and similar works have highlighted the necessity of understanding the role that the power supply circuit and vacuum chamber electrical configuration play in augmenting HET behavior to properly extrapolate to in-space conditions.

The ubiquity of the influence of the breathing mode oscillation in HET performance metrics, plasma measurements, electrical facility measurements, and anomalous electron mobility estimates highlights the importance of understanding the dynamic behavior of this oscillation and how it might differ based on the thruster environment. Towards this end, a physics-constrained extended Kalman filter (PC-EKF) is constructed to examine the dynamic behavior of key plasma properties in a HET discharge. Greve et al. [25, 26] recently showed that a similar PC-EKF is capable of producing dynamic estimates for ion and neutral number densities and electron temperature based on the ionization oscillation theories of Hara et al. [27] and Barral and Ahedo [28]. In this work, the model is extended to include electron bulk velocity, which removes the need to assume a form for the anomalous electron mobility. The effect of including an estimate of ion bulk velocity is explored, and the model is run with and without a lumped-element model of the vacuum test facility discharge circuit to investigate the electrical facility effects on the discharge plasma. Because the data used in the state estimation are taken in a vacuum test facility, the removal of the lumped-element model does not equate to an extrapolation to vacuum conditions, but does provide a qualitative illustration of how the plasma processes in the space environment would need to differ to produce the same discharge current signal.

III. Model Formulation

A zero-dimensional (0D) global plasma ionization oscillation model is used to capture the dominant breathing mode dynamics of a HET discharge plasma. Following similar global models developed by Refs. 28 and 29, the equations governing the plasma oscillations can be written as

$$\frac{\partial N_i}{\partial t} = -\frac{N_i U_i}{L_{ch}} - \frac{2 N_i U_{i,w}}{R_\Delta} + N_i N_n \zeta_{ion}, \tag{1}$$

$$\frac{\partial N_n}{\partial t} = -\frac{(N_n - N_{int}) U_n}{L_{ch}} - N_i N_n \zeta_{ion}, \tag{2}$$

$$\frac{\partial T_e}{\partial t} = \frac{2}{3 N_i} \left[-N_i U_e E - N_i \epsilon_w \nu_w - N_i N_n \zeta_{ion} \chi \epsilon_{ion} - \frac{3}{2} T_e \frac{\partial N_i}{\partial t} - \frac{5}{2} \frac{N_i U_e T_e}{L_{ch}} \right], \tag{3}$$

$$\frac{\partial U_i}{\partial t} = \frac{eE}{M_i} + \frac{2 U_{i,w} U_i}{R_\Delta} + N_n \zeta_{ion} (U_n - U_i), \tag{4}$$

$$\frac{\partial U_e}{\partial t} = 0, \tag{5}$$

where $U_{i,w} = \sqrt{eT_e/M_i}$, $N_{int} = \dot{m}(M_i A_c U_n)^{-1}$, and Eq. (5) is used in place of an assumed form for the anomalous electron mobility. The ionization rate coefficient is given as

$$\zeta_{ion} = \sqrt{\frac{8 e T_e}{\pi m_e}} \left[A T_e^2 + B \exp\left(-\frac{C}{T_e}\right) \right], \tag{6}$$

with $A = -1 \times 10^{-24}$, $B = 6.386 \times 10^{-20}$, and $C = 12.13$ [30]. The energy loss to the wall, wall collision frequency, and sheath potential are defined as

$$\epsilon_w = 2 T_e + (1 - \sigma) \phi_w, \tag{7}$$

$$\nu_w = \frac{1}{R_\Delta} \sqrt{\frac{e T_e}{M_i}} \frac{1}{1 - \sigma}, \tag{8}$$

$$\phi_w = T_e \ln \frac{1 - \sigma}{\sqrt{2\pi m_e / M_i}}, \tag{9}$$

where $\sigma = \min(T_e/25, 0.986)$, corresponding to space charge limitation at $T_e = 24.6$ eV, assuming a boron nitride channel wall [28, 30].

To couple Eqs. (1)-(5) to the discharge circuit, a lumped-element circuit model is constructed considering an ideal DC voltage source and including a low-pass filter consisting of a resistor, inductor, and capacitor. Assuming the configuration shown in Fig. 1, equations for the anode voltage, V_A, and capacitor current, I_C, can be written as

$$\frac{\partial V_A}{\partial t} = \frac{I_C}{C_f}, \tag{10}$$

$$\frac{\partial I_C}{\partial t} = \frac{1}{R_f} \left(\frac{\partial V_d}{\partial t} - \frac{\partial V_A}{\partial t} \right) + \frac{V_d - V_A}{L_f} - eA_c \left[N_i \frac{\partial U_i}{\partial t} + (U_i - U_e) \frac{\partial N_i}{\partial t} \right]. \tag{11}$$

Within this model formulation, the only coupling between the plasma processes and electrical facility is through the anode voltage. The net current at the power supply, I_{PS}, can be calculated as the sum of discharge current and capacitor current, where the discharge current is given by
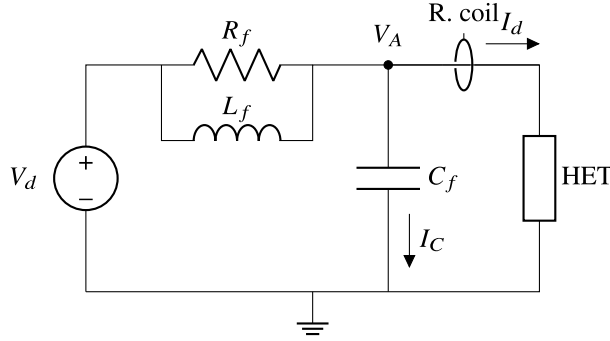
$$I_d = eA_c N_i (U_i - U_e). \tag{12}$$

Fig. 1 **Simplified schematic of the electrical configuration of the thruster and discharge circuit.** $R_f = 100~\Omega$, $L_f = 340~\mu$H, and $C_f = 8~\mu$F form the discharge filter. I_d is measured by the Rogowski coil after the discharge filter.

IV. Extended Kalman Filtering

State estimation techniques are useful for estimating quantities based on indirect measurements. The extended Kalman filter is one such method which is applicable to nonlinear systems modeled as Gaussian random processes. A thorough overview of the implementation used can be found in Ref. 25, but a brief description is provided here. In general, the EKF consists of a state vector $\boldsymbol{x}(t)$, measurement vector $\tilde{\boldsymbol{y}}(t)$, system covariance $P(t)$, measurement noise covariance $R(t)$, process noise covariance $Q(t)$, and noise gain matrix $G(t)$, where each of these quantities can be time-dependent. The noise covariances are necessary because of the inherent noise and uncertainty in both the incoming measurement data and the assumed physics model. In this work, a continuous-discrete formulation of the EKF is applied, which enables the states to be predicted based on a prescribed dynamics model. Then, at some discrete time, k, when the model acquires a incoming measurement data, denoting the predicted state and updated state with $(^-)$ and $(^+)$, respectively, the updated states can be expressed as

$$\boldsymbol{x}_k^+ = \boldsymbol{x}_k^- + K_k \left[\tilde{\boldsymbol{y}}_k - \boldsymbol{h}\left(\boldsymbol{x}_k^-\right) \right], \tag{13}$$

$$P_k^+ = [\mathbb{I} - K_k H_k(\boldsymbol{x}_k^-)] P_k^-, \tag{14}$$

where $\mathbb{I}$ is the identity matrix, $H_k\left(\boldsymbol{x}_k^-\right) = \partial \boldsymbol{h} / \partial \boldsymbol{x}_k^-$ is the measurement Jacobian matrix, and K_k is the Kalman gain, calculated as

$$K_k = P_k^- H_k^T\left(\boldsymbol{x}_k^-\right) \left[H_k\left(\boldsymbol{x}_k^-\right) P_k^- H_k^T\left(\boldsymbol{x}_k^-\right) + R_k \right]^{-1}. \tag{15}$$

Between measurement timesteps, the dynamics model is used to predict the state values as

$$\dot{x} = f(x, t), \tag{16}$$

$$\dot{P} = F(x, t)P + PF^T(x, t) + GQG^T, \tag{17}$$

where f is the dynamics model function of the state variables and $F(x, t) = \partial f / \partial x$ is the Jacobian matrix of the dynamics model.

The state variables for the EKF are taken to be $x = [N_i \ N_n \ T_e \ U_i \ U_e \ V_A \ I_C]^T$. The electron velocity U_e is not given a propagation equation (i.e., $\partial U_e / \partial t = 0$ as in Eq. 5) and therefore its value is only updated when a new measurement is taken. A discharge current signal $\tilde{I}_d$ is used as the measurement signal and is estimated as $\hat{I}_d = I_d$ as defined in Eq. (12). In this study, f is defined by Eqs. (1)-(5), (10) and (11), and G is constructed such that the process noise is only applied to the estimation of U_e.

V. Simulation Setup

Discharge current data at a sampling rate of 100 MHz are obtained via a Rogowski coil for a 1.5 kW PPS-1350 ML thruster, operated at CNRS. The walls of the discharge channel are made from BN-SiO$_2$. The thruster is operated with xenon at a flow rate of $\dot{m} = 3.5$ mg/s. Multiple datasets are collected at varying discharge voltages, with all other operating parameters unchanged. The EKF is applied to each of these current datasets, assuming the discharge voltage to be a constant value.

For all simulations, the neutral bulk velocity, U_n, is assumed to be a constant 200 m/s. The length of the thruster in the EKF is chosen to be $L_{ch} = 25$ mm and the inner and outer radii are 35 mm and 50 mm, respectively [31]. From this geometry, $A_c = 40$ cm^2 and $R_\Delta = 1.5$ cm. The ionization energy loss and ionization cost for xenon are considered to be $\epsilon_{ion} = 12.1$ eV and $\chi = 1.7$, respectively [32].

Following Ref. 25, an adaptive process noise covariance is calculated as

$$Q = \frac{P_{0,U_e} - P_{U_e}^-}{\Delta t}, \tag{18}$$

where $P_{0,U_e} = 1.1 \times 10^8$ is used as a fixed parameter for calculating the process noise covariance of the electron velocity and Δt is the timestep between consecutive measurement updates. A fixed parameter is used to ensure positivity of the process noise covariance. Though the continuous-discrete EKF allows for a variable timestep, a constant value of $\Delta t = 10$ ns is used to match the sampling frequency of the measurement signal. An adaptive noise covariance is calculated as

$$R = \beta \hat{I}_d = \beta \left[eA_c N_i \left(U_i - U_e \right) \right], \tag{19}$$

where $\beta = 0.05$ is selected such that at each timestep the noise covariance is 5% of the corresponding discharge current measurement at that timestep. A fourth-order Runge-Kutta solver is used for the physics-based model propagation. The initial conditions for the states and covariances used for each discharge current dataset are shown in Table 1. Due to the nature of the EKF, there is an initial transient during which time the state estimates converge towards their quasi-steady-state values and the covariance decreases. It is observed that fixing V_A at its initial condition (i.e., removing it as an unknown state) for some short time while the rest of the states approach stable estimates reduces the duration of this transient. In this work, the chosen duration is 20,000 timesteps, equivalent to 0.2 ms. After this time, V_A is updated with the other states.

Table 1   Initial EKF state estimates and covariances.

State	Initial value	Initial covariance
N_i (m^{-3})	1×10^{17}	1×10^{34}
N_n (m^{-3})	1×10^{19}	1×10^{36}
T_e (eV)	10	25
U_i (m/s)	$(eV_d/M_i)^{1/2}$	1×10^8
U_e (m/s)	-4×10^4	1×10^8
V_A (V)	V_d	$0.2V_d$
I_C (A)	0	5

Three mathematical systems are examined and compared. System A is a four-equation system which neglects ion momentum, using Eqs. (1)-(3), and (5). System B is a five-equation system which includes ion momentum, using Eqs. (1)-(5). System C includes the full global ionization oscillation model through Eqs. (1)-(5) and adds a coupled circuit model through Eqs. (10) and (11). In System A, the ion velocity is prescribed as $U_i = (eV_A/M_i)^{1/2}$. In Systems A and B, the anode voltage is assumed to be equivalent to the discharge voltage ($V_A = V_d$), which remains constant. The fixed states are removed from the state vector in the EKF and their dynamics are not predicted.

VI. State Estimation Results

The state estimates produced by the EKF model are shown for the case of a 200 V discharge voltage in Fig. 2. Panels (a-h) show the time series and power spectral densities (PSDs) of the discharge current, ion number density, neutral number density, electron temperature, ion bulk velocity, electron bulk velocity, anode voltage, and capacitor current, respectively. Systems A, B, and C are shown in blue, orange, and green, respectively. States that are held constant in Systems A and B are not shown, and there is significant overlap of the time series and PSDs for the three systems.
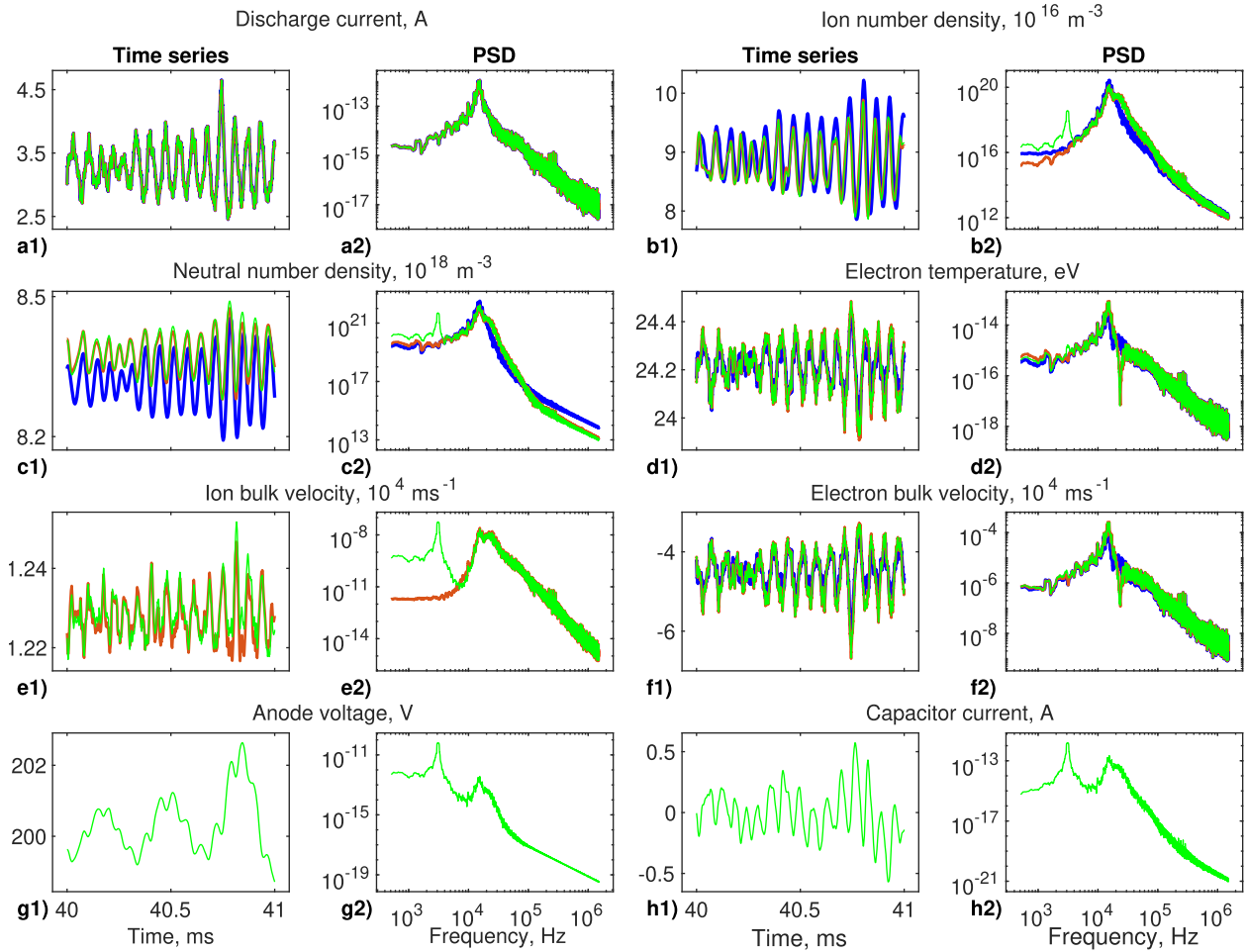

Fig. 2 EKF estimates for the 200 V dataset: (blue) System A; (orange) System B; and (green) System C. The x-axis is the same for all time series and all PSDs.

At 200 V, the inclusion of the ion momentum leads to an insignificant change in amplitude at the dominant oscillation frequency in all states. However, one notable change shown in Figs. 2(d2,f2) is that the PSD dips near 17.8 kHz for System A but a sharper dip exists at a slightly higher frequency of 23.1 kHz for Systems B and C. The decreases in spectral density seen in System A occur very close to the harmonic frequency of a two-equation predator-prey system, approximated as $\omega_b = (N_{i,0}N_{n,0}\zeta_{ion,0}^2)^{1/2}$, where the "0" subscript indicates the equilibrium value each quantity [15]. Here, the equilibrium value is calculated as the mean of the time history of each state. Because the simplest model used

here has more than two equations, the true harmonics of the systems studied will differ somewhat from this value of ω_b.

In the two-equation predator-prey system [15], a resonance would be expected at the harmonic frequency. However, when coupled with the EKF, oscillations will be enforced at the frequency of the peak spectral density in the discharge current signal, which may not be the same as the harmonic in the mathematical system. Equation (12) includes a product of N_i and $(U_i - U_e)$, and on average $|U_e| > |U_i|$. Because the harmonic frequency of the mathematical system leads to a resonance which is absent in the measured data, a peak must occur in one state and a dip in the other. When state estimates are multiplied, the mode is suppressed in the resulting discharge current estimate. The appearance of this peak in N_i can be seen clearly in Fig. 2(a2), accompanied by the dip in U_e in Fig. 2(f2). Though predicting the harmonic frequencies as more equations are added to the model becomes increasingly complex, it is likely that the inclusion of the ion momentum modifies the harmonic frequency of the system, shifting the location of the peak and dip in the PSDs. Oscillations at this frequency can be observed in all states.

More notably, the inclusion of the circuit effects in System C leads to a clear peak in spectral density at approximately 3 kHz, which corresponds to the resonant frequency of the low-pass filter included in the circuit model. The unsteady oscillation amplitude of the anode voltage is on the order of 1-2 V and the oscillation is dominated by the 3 kHz circuit frequency. Lower amplitude oscillations are also visible at the breathing mode frequency. The capacitor current is found to oscillate with a maximum amplitude of approximately 0.5 A and is zero-mean, which is consistent with the zero current expected in DC operation.
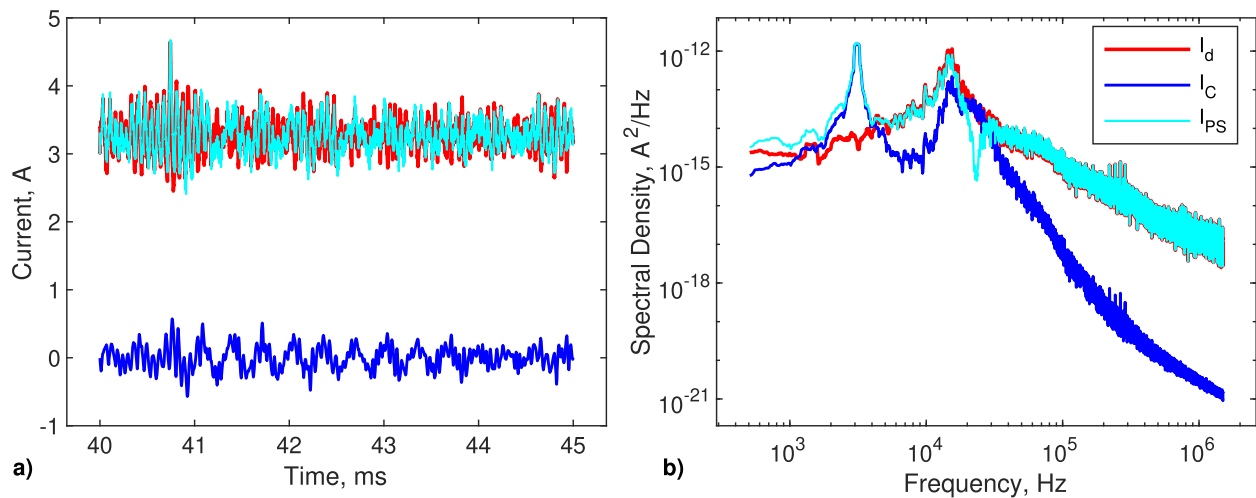

Fig. 3   Discharge (red), capacitor (blue), and power supply (light blue) currents estimated and calculated from the 200 V case.

Figure 3 compares the capacitor current to the thruster discharge current and the power supply current for the 200 V discharge voltage case. It can be seen from Fig. 3(a) that the the power supply current contains oscillatory components at both the circuit resonant frequency and the breathing mode frequency. While the magnitude of oscillations at the breathing mode frequency is slightly attenuated by the capacitor in Fig. 3(b), the fact that a strong oscillation is still present suggests that the lumped-element model may be insufficient to accurately describe the interaction between the discharge filter and discharge current. Interestingly, there is strong attenuation at the harmonic frequency seen in Figs. 2(d2,f2). Maximum attenuation will occur when the discharge and capacitor currents are 180 degrees out of phase with one another.

The state estimates for the 350 V discharge voltage case are shown in Fig. 4 in the same manner as in Fig. 2. Similar decreases in the PSDs of U_e are seen in Fig. 4(d2,f2) as those in Fig. 2(d2,f2), though now at frequencies of 16.7 kHz and 22.9 kHz and with a shallower dip. A sharp dip is still observed in the PSD of T_e at this frequency. The general impact of including the ion momentum equation appears to be consistent for all discharge voltages examined.

The interaction between the circuit and the state estimates appears stronger in the 350 V case than for any other discharge voltage, and clear peaks are visible in the PSDs of each state. The amplitudes of the anode voltage and capacitor current oscillations vary in non-sinusoidal patterns over time-scales governed by the resonant frequency of the circuit. Though the maximum peak-to-peak oscillations shown in Fig. 4 are 40 V and 7 A, the maximum throughout the 6.5 ms of data examined reaches 95 V and 15 A. Similarly large peak-to-peak values are reported by Ref. [24],
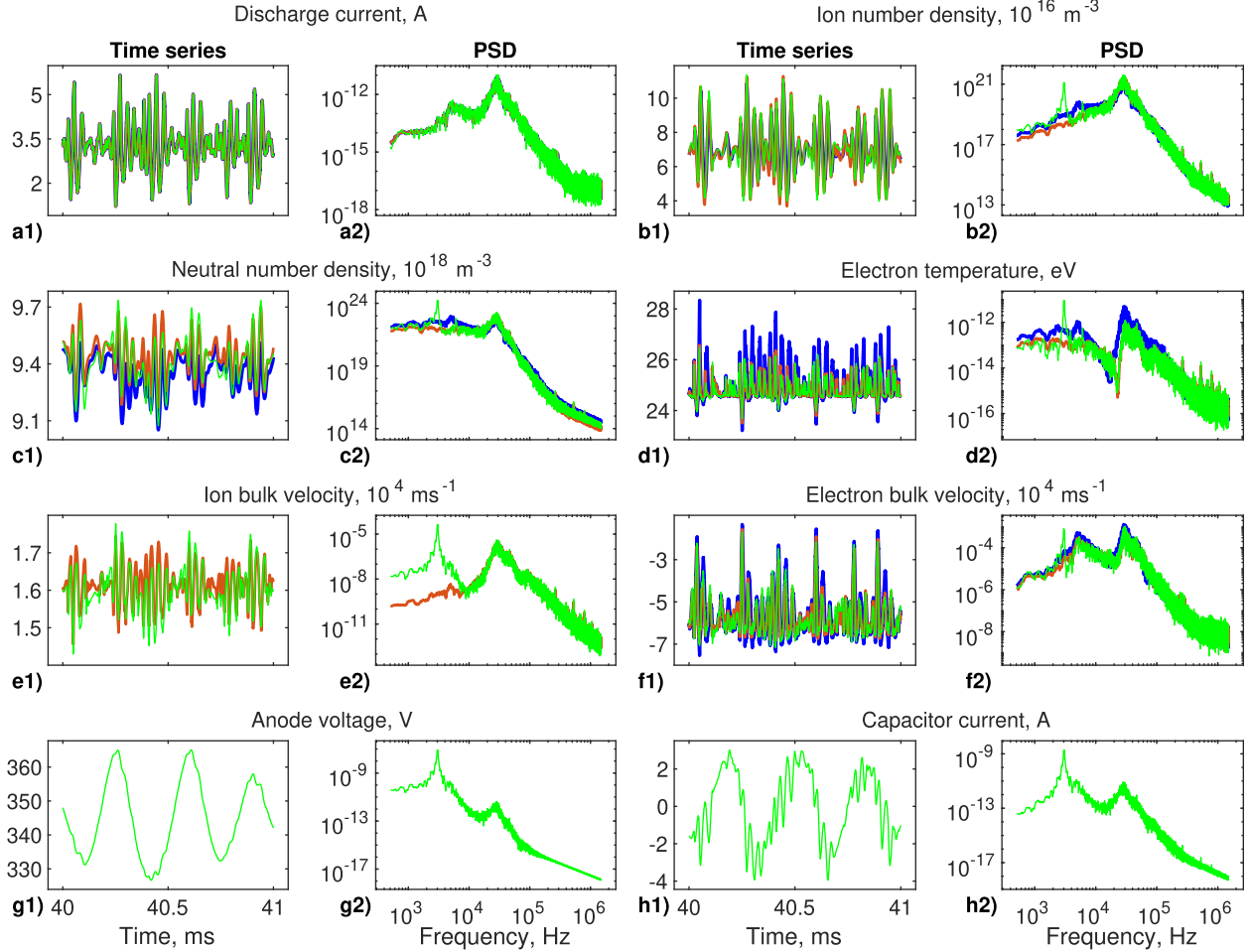
7

Fig. 4 EKF estimates for the 350 V dataset: (blue) System A; (orange) System B; and (green) System C; The x-axis is the same for all time series and all PSDs.

in which it was observed oscillations up to 174 V with the HERMeS thruster operating at 600 V and 12.5 kW. The significant interaction between the circuit and state estimates observed here can perhaps be explained by the broad low-frequency bump visible in Fig. 4(a2), which peaks near the first harmonic of the discharge filter resonant frequency (approximately 6 kHz). A strong excitation of oscillations in both N_i and U_e at the filter resonant frequency then excites the first harmonic, which can be seen to have a broad distribution in Fig. 4(f2).

Figure 5 shows the discharge, capacitor, and power supply currents along with their PSDs for the 350 V discharge voltage case. As with the 200 V case, Fig. 5(b) shows a clear peak in spectral density at the circuit resonant frequency for both capacitor and power supply current. At 350 V, the attenuation of the breathing mode peak in the power supply current is more significant, suggesting that the model is better able to capture the expected filtering. A more significant attenuation is again observed at the harmonic frequency.

Though not shown, the results for the circuit parameters are qualitatively similar in all cases. With the exception of the 350 V case, the maximum amplitude of the anode voltage oscillation does not exceed 5% of the mean value and the amplitude of the capacitor current oscillations does not exceed 3 A. The anode voltage oscillations tend to be dominated by the circuit resonant frequency more than the discharge capacitor oscillations.

VII. Conclusions & Future Work

A 0D global plasma ionization oscillation model, coupled with a lumped-element circuit model of the discharge circuit of a test facility, is implemented as a set of physics-based constraints for an EKF model of a HET discharge plasma. Ion and neutral number density, ion and electron bulk velocities, electron temperature, anode voltage, and
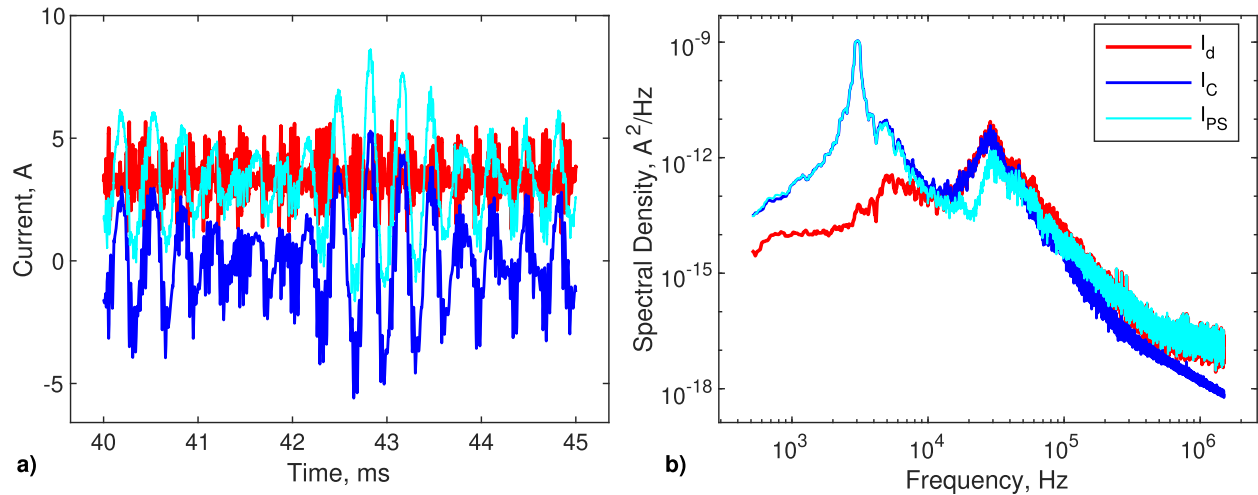
Fig. 5   Discharge (red), capacitor (blue), and power supply (light blue) currents estimated and calculated from the 350 V case.

discharge filter capacitor current are estimated using discharge current as the measurement signal. Three system models are compared: a four-equation system that only considers the ion and neutral number densities, electron temperature, and electron bulk velocity; a five-equation system that adds the ion momentum equation, estimating ion bulk velocity; and a seven-equation system that includes facility discharge circuit effects. The unused states in the four- and five-equation models are held fixed and not estimated by the EKF.

It is observed that the ion momentum equation leads to a 4-6 kHz shift in the harmonic frequency estimated by mathematical systems describing the ionization oscillations, but that this frequency does not necessarily align with the dominant measured breathing mode frequency. This harmonic frequency remains between 16-18 kHz for the four-equation system, and between 22-24 kHz for the five- and seven-equation systems. It leads to a local increase in the spectral density of N_i and decrease in that of U_e, which then affects the estimated values of the other states. In contrast, the experimentally measured breathing mode varies as expected with discharge voltage.

The addition of circuit effects into the seven-equation system introduces a low-frequency mode into many of the estimated states across the range of discharge voltages studied. These results demonstrate that dynamic plasma properties can be estimated in a way that takes into account the effects of the discharge circuit and that these effects may be significant. While the 0D plasma model and lumped-element circuit model are approximations of more complicated systems, the presented model demonstrates that the interaction between these systems can be effectively studied using experimental data. Future work may expand the robustness of the plasma model to better align the predicted and measured harmonic frequencies. Improvements to the electrical facility model can be made by considering a more complete power supply circuit and including the electron and ion pathways between the thruster, plume, and vacuum chamber walls.

Acknowledgments

References

[1] Zhurin, V., Kahn, J., Kaufman, H., Kozubsky, K., and Day, M., "Dynamic characteristics of closed drift thrusters," *23rd International Electric Propulsion Conference*, 1993. IEPC-1993-095.

[2] Choueiri, E. Y., "Plasma oscillations in Hall thrusters," *Physics of Plasmas*, Vol. 8, No. 4, 2001, pp. 1411–1426. https://doi.org/10.1063/1.1354644.

9

[3] Gascon, N., Dudeck, M., and Barral, S., "Wall material effects in stationary plasma thrusters. I. Parametric studies of an SPT-100," *Physics of Plasmas*, Vol. 10, No. 10, 2003, pp. 4123–4136. https://doi.org/10.1063/1.1611880.

[4] Mikellides, I. G., and Katz, I., "Numerical simulations of Hall-effect plasma accelerators on a magnetic-field-aligned mesh," *Phys. Rev. E*, Vol. 86, 2012, p. 046703. https://doi.org/10.1103/PhysRevE.86.046703.

[5] Katz, I., Mikellides, I. G., Jorns, B. A., and Ortega, A. L., "Hall2De simulations with an anomalous transport model based on the electron cyclotron drift instability," *34th International Electric Propulsion Conference*, Vol. 402, 2015.

[6] Hara, K., and Mikellides, I. G., *Characterization of low frequency ionization oscillations in Hall thrusters using a one-dimensional fluid model*, 2018. https://doi.org/10.2514/6.2018-4904.

[7] Hara, K., "An overview of discharge plasma modeling for Hall effect thrusters," *Plasma Sources Science and Technology*, Vol. 28, No. 4, 2019, p. 044001. https://doi.org/10.1088/1361-6595/ab0f70.

[8] Lobbia, R. B., and Gallimore, A. D., "Two-dimensional time-resolved breathing mode plasma fluctuation variation with Hall thruster discharge settings," *31st International Electric Propulsion Conference*, Ann Arbor, MI, USA, 2009. IEPC-2009-106.

[9] Lobbia, R. B., and Gallimore, A. D., "High-speed dual Langmuir probe," *Review of Scientific Instruments*, Vol. 81, No. 7, 2010, p. 073503. https://doi.org/10.1063/1.3455201.

[10] Giannetti, V., Saravia, M. M., and Andreussi, T., "Measurement of the breathing mode oscillations in Hall thruster plasmas with a fast-diving triple Langmuir probe," *Physics of Plasmas*, Vol. 27, No. 12, 2020, p. 123502. https://doi.org/10.1063/5.0022928.

[11] Wei, L., Li, W., Ding, Y., and Yu, D., "Effect of low-frequency oscillation on performance of Hall thrusters," *Plasma Science and Technology*, Vol. 20, No. 7, 2018, p. 075502. https://doi.org/10.1088/2058-6272/aabae0.

[12] Mullins, C. R., Farnell, C. C., Farnell, C. C., Martinez, R. A., Liu, D., Branam, R. D., and Williams, J. D., "Non-invasive Hall current distribution measurement in a Hall effect thruster," *Review of Scientific Instruments*, Vol. 88, No. 1, 2017, p. 013507. https://doi.org/10.1063/1.4974098.

[13] Dale, E. T., and Jorns, B. A., "Non-invasive time-resolved measurements of anomalous collision frequency in a Hall thruster," *Physics of Plasmas*, Vol. 26, No. 1, 2019, p. 013516. https://doi.org/10.1063/1.5077008.

[14] Kaganovich, I. D., Raitses, Y., Sydorenko, D., and Smolyakov, A., "Kinetic effects in a Hall thruster discharge," *Physics of Plasmas*, Vol. 14, No. 5, 2007, p. 057104. https://doi.org/10.1063/1.2709865.

[15] Fife, J. M., "Two-Dimensional Hybrid Particle-In-Cell Modeling of Hall Thrusters," Ph.D. thesis, Massachusetts Institute of Technology, Cambridge, MA, 1995.

[16] Cappelli, M. A., Young, C. V., Cha, E., and Fernandez, E., "A zero-equation turbulence model for two-dimensional hybrid Hall thruster simulations," *Physics of Plasmas*, Vol. 22, No. 11, 2015, p. 114505. https://doi.org/10.1063/1.4935891.

[17] Lafleur, T., Baalrud, S. D., and Chabert, P., "Theory for the anomalous electron transport in Hall effect thrusters. I. Insights from particle-in-cell simulations," *Physics of Plasmas*, Vol. 23, No. 5, 2016, p. 053502. https://doi.org/10.1063/1.4948495.

[18] Lafleur, T., Baalrud, S. D., and Chabert, P., "Theory for the anomalous electron transport in Hall effect thrusters. II. Kinetic model," *Physics of Plasmas*, Vol. 23, No. 5, 2016, p. 053503. https://doi.org/10.1063/1.4948496.

[19] Jorns, B., "Predictive, data-driven model for the anomalous electron collision frequency in a Hall effect thruster," *Plasma Sources Science and Technology*, Vol. 27, No. 10, 2018. https://doi.org/10.1088/1361-6595.

[20] Koo, J. W., and Boyd, I. D., "Modeling of anomalous electron mobility in Hall thrusters," *Physics of Plasmas*, Vol. 13, No. 3, 2006, p. 033501. https://doi.org/10.1063/1.2172191.

[21] Frieman, J. D., King, S. T., Walker, M. L. R., Khayms, V., and King, D., "Role of a Conducting Vacuum Chamber in the Hall Effect Thruster Electrical Circuit," *Journal of Propulsion and Power*, Vol. 30, No. 6, 2014, pp. 1471–1479. https://doi.org/10.2514/1.B35308.

[22] Walker, J. A., Frieman, J. D., Walker, M. L. R., Khayms, V., King, D., and Peterson, P. Y., "Electrical Facility Effects on Hall-Effect-Thruster Cathode Coupling: Discharge Oscillations and Facility Coupling," *Journal of Propulsion and Power*, Vol. 32, No. 4, 2016, pp. 844–855. https://doi.org/10.2514/1.B35835.

[23] Peterson, P. Y., Kamhawi, H., Huang, W., Williams, G., Gilland, J. H., Yim, J., Hofer, R. R., and Herman, D. A., "NASA HERMeS Hall Thruster Electrical Configuration Characterization," *52nd AIAA/SAE/ASEE Joint Propulsion Conference*, 2016, p. 5027.

[24] Piñero, L. R., "The Impact of Harness Impedance on Hall Thruster Discharge Oscillations," *35th International Electric Propulsion Conference*, Atlanta, GA, USA, 2017. IEPC-2017-023.

[25] Greve, C. M., Majji, M., and Hara, K., "Real-time state estimation of low-frequency plasma oscillations in Hall effect thrusters," *Physics of Plasmas*, Vol. 28, No. 9, 2021, p. 093509. https://doi.org/10.1063/5.0057751.

[26] Greve, C., and Hara, K., "Estimation of Plasma Properties Using an Extended Kalman Filter with Plasma Global Models," *Journal of Physics D: Applied Physics*, 2022. In press.

[27] Hara, K., Sekerak, M. J., Boyd, I. D., and Gallimore, A. D., "Perturbation analysis of ionization oscillations in Hall effect thrusters," *Physics of Plasmas*, Vol. 21, No. 12, 2014, p. 122103. https://doi.org/10.1063/1.4903843.

[28] Barral, S., and Ahedo, E., "Theoretical study of the breathing mode in Hall thrusters," *42nd AIAA/ASME/SAE/ASEE Joint Propulsion Conference & Exhibit*, 2006, p. 5172.

[29] Hara, K., Keller, S., and Raitses, Y., "Measurements and theory of driven breathing oscillations in a Hall effect thruster," *52nd AIAA/SAE/ASEE Joint Propulsion Conference*, 2016. https://doi.org/10.2514/6.2016-4532.

[30] Goebel, D., and Katz, I., *Fundamentals of Electric Propulsion: Ion and Hall Thrusters*, Wiley, Hoboken, NJ, 2008.

[31] Boeuf, J. P., and Garrigues, L., "Low frequency oscillations in a stationary plasma thruster," *Journal of Applied Physics*, Vol. 84, No. 7, 1998, pp. 3541–3554. https://doi.org/10.1063/1.368529.

[32] Hara, K., Sekerak, M. J., Boyd, I. D., and Gallimore, A. D., "Mode transition of a Hall thruster discharge plasma," *Journal of Applied Physics*, Vol. 115, No. 20, 2014, p. 203304. https://doi.org/10.1063/1.4879896.